

Composite Molecular Assemblies: Nanoscale Structural Control and Spectroelectrochemical Diversity

Graham de Ruiter,[†] Michal Lahav,[†] Guennadi Evmenenko,^{‡,§} Pulak Dutta,[‡] Domenico A. Cristaldi,^{||} Antonino Gulino,^{||} and Milko E. van der Boom^{†,*}

[†]Department of Organic Chemistry, The Weizmann Institute of Science, 76100 Rehovot, Israel,

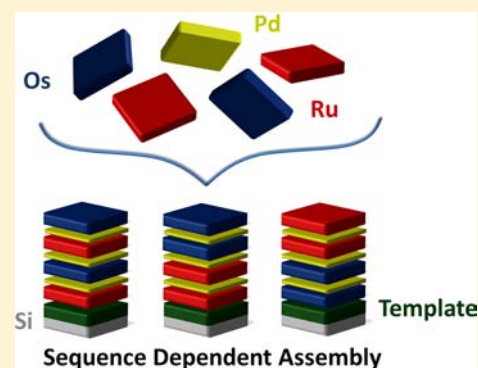
[‡]Department of Physics and Astronomy, Northwestern University, Evanston, Illinois 60208-3112, United States,

[§]Department of Materials Science and Engineering, Northwestern University, Evanston, Illinois 60208-3108, United States, and

^{||}Dipartimento di Scienze Chimiche, Università di Catania, Catania 95125, Italy

S Supporting Information

ABSTRACT: The controlled deposition of metal complexes from solution on inorganic surfaces offers access to functional materials that otherwise would be elusive. For such surface-confined interfaces to form, specific assembly sequences are often used. We show here that varying the assembly sequence of two well-defined and iso-structural osmium and ruthenium polypyridyl complexes results in interfaces with strikingly different spectroelectrochemical properties. Successive deposition of redox-active layers of osmium and ruthenium polypyridyl complexes, leads to self-propagating molecular assemblies (SPMAs) with distinct internal interfaces and individually addressable components. In contrast, the clear separation of these interfaces upon sequential deposition of these two complexes, results in charge trapping or electrochemical communication between the metal centers, as a function of layer thickness and applied assembly sequence. The SPMAs were characterized using a variety of techniques, including: UV–vis spectroscopy, spectroscopic ellipsometry, electrochemistry, synchrotron X-ray reflectivity, angle-resolved X-ray photoelectron spectroscopy, and spectroelectrochemistry. The combined data demonstrate that the sequence-dependent assembly is a decisive factor that influences and provides the material properties that are difficult to obtain otherwise.



1. INTRODUCTION

Understanding the many variables involved in forming supramolecular structures using metal–ligand coordination is often challenging. Factors like coordination number and geometry together with the nature of the ligand and the metal salt are but a few examples that are important in the complex niche of coordination chemistry.¹ Variation of the above-mentioned parameters has led to numerous fascinating structures.^{1,2} Nitschke et al. demonstrated the formation of copper and zinc helicates in solution, whose stability not only depends on the ratio of the ligands, but also on the addition sequence.^{3,4} The delicate interplay between those parameters resulted in dynamic self-assembly processes, able to cascade chemical transformations similar to signal transduction cascades in biology.³ Stang et al., reported various well-defined shapes such as triangles, squares, rectangles, and three-dimensional structures such as cubes, by considering the geometrical constraints implied by the ligands and metal salts.^{5–7} In the past decade, these principles have also been extended to surface-chemistry by others.^{8–19} The chemical modification of inorganic surfaces is an important development in the ongoing research toward hybrid functional materials. Diverse materials have been obtained that have found applications in sensors,^{20,21} electro-optics,^{22,23} photovoltaics,²⁴ catalysis,²⁵ and organic field

effect transistors (OFETs),^{26,27} among others. Although there are established techniques available for surface modification,^{28–35} layer-by-layer (LbL) assembly from solution is attractive, as it offers many advantages. For instance, multiple molecular building blocks can be incorporated in a highly ordered and structured manner by utilizing directional intermolecular forces such as hydrogen bonding, π – π stacking, and electrostatic, dipole–dipole or van der Waals interactions.^{36–40} The information that is encoded in the molecular building blocks—by means of their geometry and intermolecular interactions—govern the resulting supramolecular structures.⁶ Furthermore, LbL film growth allows for sequences to be developed to arrange the molecular entities inside the supramolecular structures. Often conserved assembly sequences are used without varying the assembly sequence. Recent examples of molecular programming with molecular assembly surfaces are (i) the formation of molecular wires by Nishihara with terpyridine compounds of Fe and Co and (ii) the multilayers of Unger and Schalley.^{41,42} However, to demonstrate control over the sequence in which the molecules are arranged in an assembly is of critical importance for governing

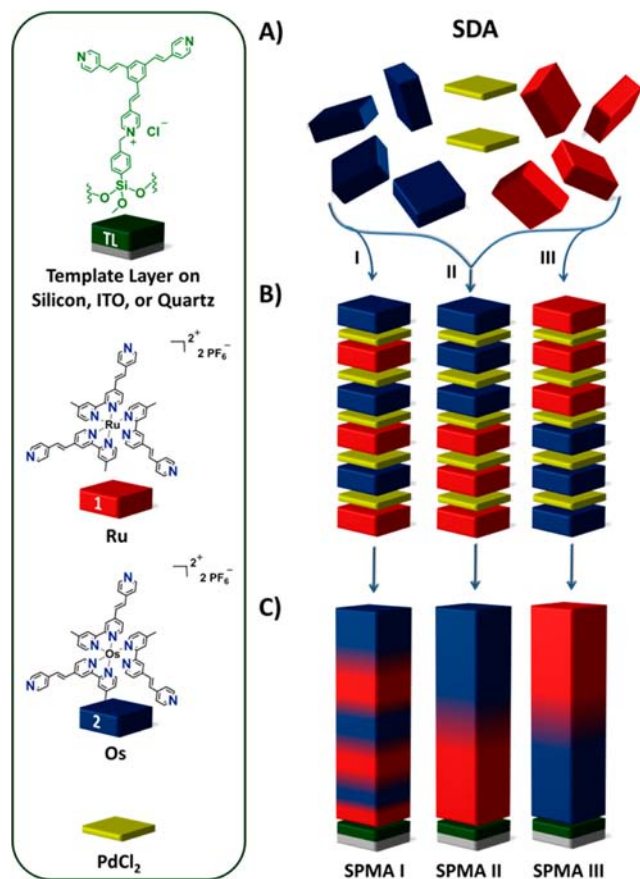
Received: July 30, 2013

Published: October 25, 2013

their material properties. Such a molecular control can be implemented by a using sequence-dependent assembly (SDA).⁴³ Biology makes extensive use of this principle, for instance in cis-regulatory elements in DNA.⁴⁴

In the present study, we show how the internal composition and properties of the SPMAs (I–III) can be controlled by an SDA. For our SDA, we use polypyridyl complexes **1** and **2**. These ruthenium (**1**) and osmium (**2**) complexes are highly stable and are known to exhibit reversible electrochromic behavior by electrochemically changing their oxidation state from $M^{2+} \rightarrow M^{3+}$ ($M = \text{Os}, \text{Ru}$).^{43,45} These type of iso-structural and iso-electronic complexes are used in dye-sensitized solar cells^{46–48} and electroluminescent devices.^{49,50} The SDA follows an iterative deposition procedure illustrated in Scheme 1. X-ray photoelectron spectroscopy (XPS) and X-ray reflectivity (XRR) revealed how the assembly of two metal

Scheme 1. Sequence-Dependent Assembly (SDA) of the Self-Propagating Molecular Assemblies (SPMAs) I–III^a



^aThe interfaces are formed by immersion of a pyridine-terminated template layer⁵¹ on quartz, silicon, and ITO-coated glass substrates. The SPMAs consist of three main components: a ruthenium complex **1**, an osmium complex **2**, and a $\text{Pd}(\text{PhCN})_2\text{Cl}_2$ (A). The SPMAs are differentiated by three different assembly sequences; (i) repetitive alternate immersion of the pyridine template layer in a solution of **1** followed by **2**, (ii) sequential immersion in a solution of **1** followed by **2**, or (iii) sequential immersion in a solution of **2**, followed by **1** (B). The resulting SPMAs (C) all employ the same assembly strategy, which involves immersion of the pyridine-terminated template layers in a 1.0 mM THF solution of $\text{Pd}(\text{PhCN})_2\text{Cl}_2$, followed by immersion in 0.2 mM solutions of complexes **1** or **2** in THF/DMF (9:1 v/v) according to their respective SDA.

complexes (**1**, **2**) resulted in distinct interfaces with well-defined thicknesses and a low surface roughness. The defined interfaces combined with the use of iso-structural metal complexes allow for continues assembly formation with a near homogeneous electron density, with little intermixing of the metal complexes at the Ru/Os or Os/Ru interface. Although the SPMAs show nearly identical optical properties and uniformity in their electron-density, each SPMA exhibit a different distribution of oxidation potentials through-out the assembly. Reversible electrochemical behavior is observed when the interfaces are below a certain threshold thickness (>8.0 nm) regardless of the oxidation potential and composition of the interfaces. In contrast, oxidative catalytic electrochemical behavior is observed when a uniform interface is formed with a high oxidation potential, followed by an interface with a lower oxidation potential. This electrochemical behavior can be reversed, by reversing the assembly order of the interfaces, i.e., by first assembling a uniform interface with a low oxidation potential, followed by an interface with a higher oxidation potential. The relationship between the internal composition, distribution of oxidation potentials and the thickness of these interfaces is elucidated by means of differences in the electrochemistry and spectroelectrochemistry. This establishes the direct link, and importance, of the internal composition and applied SDA strategies for SPMAs.

2. RESULTS AND DISCUSSION

2.1. Molecular Assembly Formation. The SPMAs were formed by immersing pyridine-terminated template layers in a 1.0 mM THF solution of $\text{trans-Pd}(\text{PhCN})_2\text{Cl}_2$ to allow for the coordination of PdCl_2 .⁵¹ This enables the first deposition of one of the metal complexes (**1**, **2**) on indium tin oxide (ITO), quartz, or silicon. Iterative immersion in a THF solution of $\text{Pd}(\text{PhCN})_2\text{Cl}_2$, followed by immersion in a THF/DMF (9:1) solution containing the metal polypyridyl complex **1** or **2** (0.2 mM) resulted in formation of SPMAs with various compositions. We demonstrated here three possible assembly sequences: (i) alternating deposition of **1** and **2**; (ii) successive deposition of **1**, followed by **2**; or (iii) successive deposition of **2**, followed by **1**.⁴³ As a result, the SPMAs only differ in the internal ordering of the used metal complexes (Scheme 1). In accordance with the assembly strategy the names of the SPMAs coincide. SPMA I | $\text{Ru}_x\text{-Os}_y$, SPMA II | $\text{Ru}_x\text{-Os}_y$, and SPMA III | $\text{Os}_x\text{-Ru}_y$, refer to SDA I, II, and III, where x and y denote the number of depositions steps in which complexes **1** (Ru) or **2** (Os) were deposited.

2.2. UV–vis Spectroscopy and Spectroscopic Ellipsometry. The growth of the SPMAs was followed by UV–vis spectroscopy with SPMAs formed on quartz substrates. The absorption spectra of complexes **1** and **2** are nearly identical (Figure S1 of the Supporting Information, SI). Both exhibit a strong absorption in the UV-region, at approximately $\lambda = 320$ nm. This absorption is characteristic for a ligand centered $\pi\text{-}\pi^*$ transition.^{52,53} A broad absorption band in the visible region is observed between $\lambda = 400\text{--}550$ nm, which is the spin-allowed singlet–singlet transition from the ground state to the first excited state.^{52,53} This metal-to-ligand charge-transfer (¹MLCT) band is characteristic for complexes of the type $[\text{M}(\text{bpy})_3][\text{PF}_6]_2$, where $\text{M} = \text{Os}, \text{Ru}, \text{or Fe}$.^{52–54} For complexes **1** and **2**, the maximum absorption intensity of the ¹MLCT bands are found at $\lambda = 490$ and 510 nm, respectively. In addition, the absorption spectra of **2**, exhibits an additional ³MLCT band between $\lambda = 600\text{--}750$ nm, which is not present

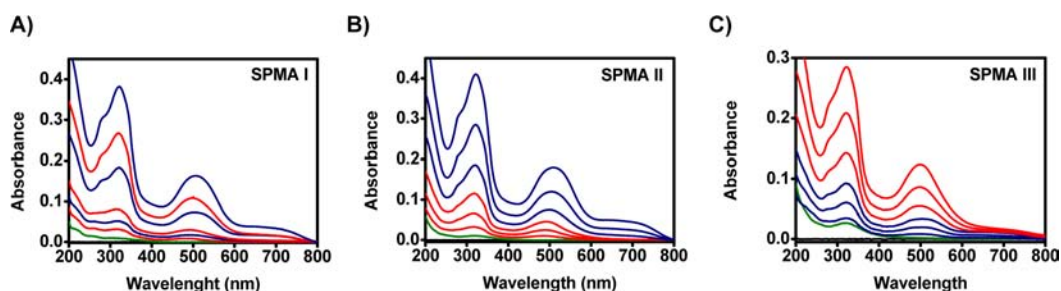


Figure 1. Optical absorption spectra of SPMA on quartz formed by SDA I–III. (A) SPMA I | $\text{Ru}_3\text{-Os}_3$, (B) SPMA II | $\text{Ru}_3\text{-Os}_3$, and (C) SPMA III | $\text{Os}_3\text{-Ru}_3$, with thicknesses of 20.3, 24.6, and 17.9 nm. The red and blue traces correspond to UV–vis spectra taken after the deposition steps that contained metal complexes 1 (Ru) or 2 (Os), respectively. The green trace represents the template layer (Scheme 1).

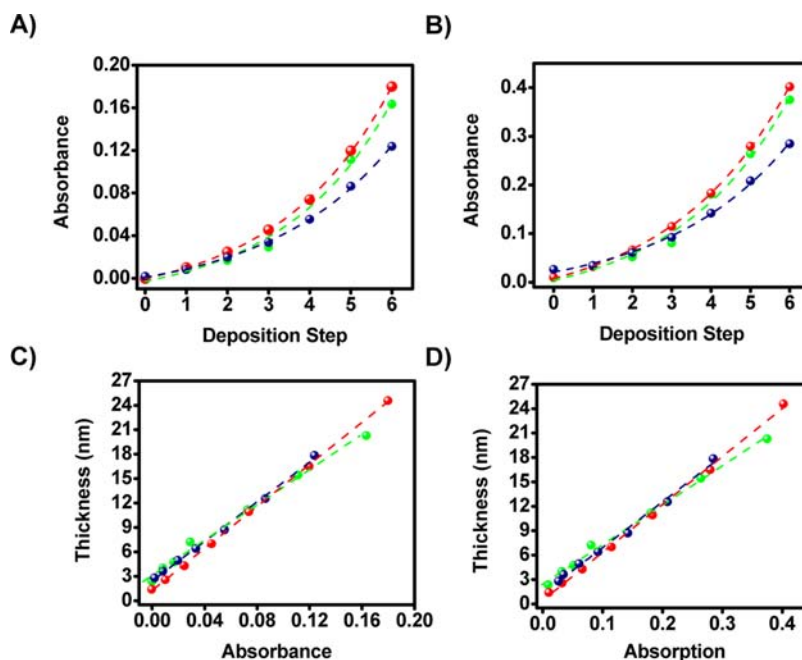


Figure 2. Optical absorbance and ellipsometry data of SPMA I | $\text{Ru}_3\text{-Os}_3$ (green ●), SPMA II | $\text{Ru}_3\text{-Os}_3$ (red ●), and SPMA III | $\text{Os}_3\text{-Ru}_3$ (blue ●) on quartz and silicon substrates. Comparison of the metal-to-ligand charge-transfer ($^1\text{MLCT}$) band at $\lambda = 500$ nm (A), and the $\pi\text{-}\pi^*$ band at $\lambda = 319$ nm (B) as a function of the number of deposition steps; and a comparison of spectroscopic ellipsometry derived thickness vs optical absorption of the $^1\text{MLCT}$ band at $\lambda = 500$ nm (C), and the $\pi\text{-}\pi^*$ band at $\lambda = 319$ nm (D). All SPMA show an exponential correlation (A and B) between the number of deposition steps and the thickness; or a linear correlation (C and D) between the thickness and the absorption of the $^1\text{MLCT}$ or $\pi\text{-}\pi^*$ band, respectively. All $R^2 > 0.99$.

in the ruthenium analog **1**. The appearance of the $^3\text{MLCT}$ is due to the large spin–orbit coupling of the osmium atom that allows for the principal spin-forbidden singlet–triplet transition to occur.^{55,56} Since the SPMA consist of a mixture of metal complexes **1** and **2**, their optical spectra is expected to be the sum of their individual components. Indeed, the $\pi\text{-}\pi^*$, $^1\text{MLCT}$, and $^3\text{MLCT}$ band are clearly visible in the UV–vis spectra of SPMA I | $\text{Ru}_3\text{-Os}_3$, SPMA II | $\text{Ru}_3\text{-Os}_3$, and SPMA III | $\text{Os}_3\text{-Ru}_3$ (Figure 1). The $^3\text{MLCT}$ band permits us to examine the growth and the content of the osmium complex **2** in the SPMA, without interference of complex **1**. As a result, monitoring the growth of SPMA I | $\text{Ru}_3\text{-Os}_3$ at $\lambda = 700$ nm, revealed a stepwise increase in the absorption of the $^3\text{MLCT}$ band, which coincides with the alternating deposition of the Ru (**1**) and Os (**2**) complexes (Figure S2 of the SI).

Upon formation of SPMA I | $\text{Ru}_3\text{-Os}_3$, SPMA II | $\text{Ru}_3\text{-Os}_3$, and SPMA III | $\text{Os}_3\text{-Ru}_3$, the λ_{max} of the $^1\text{MLCT}$ either alternates (SPMA I) or exhibits a bathochromic (SPMA II) or hypsochromic (SPMA III) shift (Figure 1). The change in

$^1\text{MLCT}$ occurs according to the character of the metal complex, i.e., the λ_{max} of the $^1\text{MLCT}$ band will either shift more to 490 nm (**1**; Ru) or 510 nm (**2**; Os).

Monitoring the $^1\text{MLCT}$ and $\pi\text{-}\pi^*$ bands centered at $\lambda = 500$ nm and $\lambda = 317$ nm respectively, revealed an exponential growth behavior for all three types of SPMA (Figure 2). Exponential growth has also been observed by us in monometallic molecular assemblies. Polyelectrolytes are also known to show nonlinear growth.^{57–60} The porous nature of the SPMA allows the storage of an excess of palladium, which is able to diffuse outward in subsequent deposition steps. Since the formed diffusion layer is dependent on the thickness of the assemblies, in each subsequent step more palladium can be stored; and exponential growth is observed.^{15,61} Since the diffusion involves the metal salt, changes in the metal center, and/or ligands can change the nature of the growth of the SPMA.⁶² Furthermore, the exposure time to $\text{Pd}(\text{PhCN})_2\text{Cl}_2$ was found to be important as well.⁶¹ Since all parameters were kept constant in this study and only the assembly sequence is

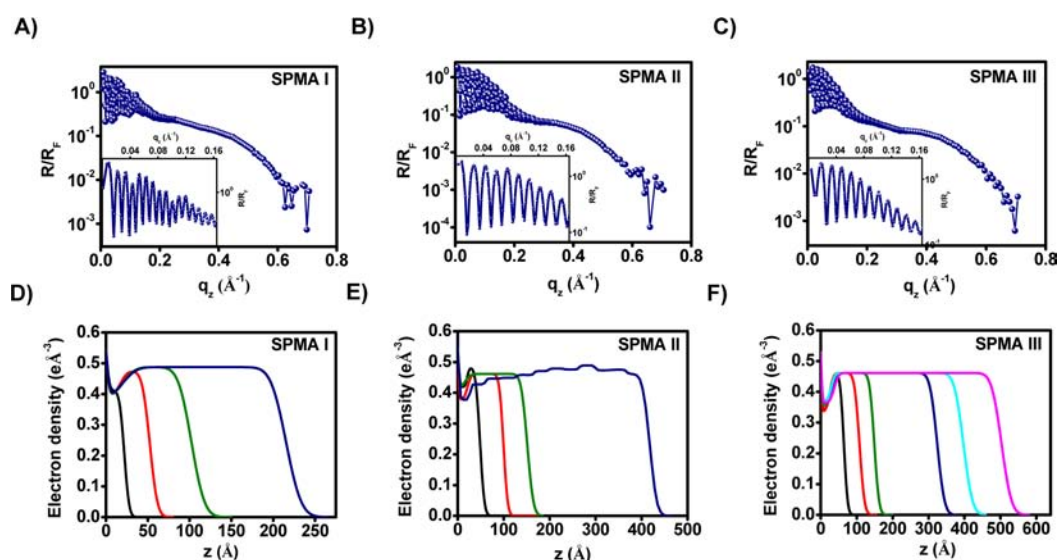


Figure 3. Representative synchrotron specular X-ray reflectivity (XRR) data of SPMA I | Ru₆-Os₆ (A), SPMA II | Ru₄-Os₄ (B), and SPMA III | Os₄-Ru₄ (C), with XRR-derived thicknesses of 64.2, 40.4, and 46.4 nm. The reflectivity R is normalized to the Fresnel reflectivity R_F . The insets show an enlargement of the Kiessig fringes observed in all SPMAs. Parts D–F show the electron density profiles for (D) SPMA I | Ru₁-Os₁ (red trace), SPMA I | Ru₂-Os₂ (green trace), SPMA I | Ru₃-Os₃ (blue trace), and template layer (black trace; scheme 1) as a function of the film thickness; (E) for SPMA II | Ru₂-Os₀ (black trace), SPMA II | Ru₄-Os₀ (red trace), SPMA II | Ru₄-Os₂ (green trace), and SPMA II | Ru₄-Os₄ (blue trace) as a function of the film thickness; and (F) for SPMA III | Os₂-Ru₀ (black trace), SPMA III | Os₄-Ru₀ (red trace), SPMA III | Os₄-Ru₁ (green trace), SPMA III | Os₄-Ru₂ (blue trace), SPMA III | Os₄-Ru₃ (magenta trace), and SPMA III | Os₄-Ru₄ (purple trace) as a function of the film thickness. For details regarding the analysis of XRR data, see refs 65 and 66.

Table 1. Structural Parameters of SPMAs Created by the SDAs According to Scheme 1^a

SPMA I					SPMA II					SPMA III				
entry	$\sigma_{\text{film-air}}$ (nm)	T_{film} (nm) ^b	T_{film} (nm) ^c	ρ_{film} (eÅ ⁻³)	entry	$\sigma_{\text{film-air}}$ (nm)	T_{film} (nm) ^b	T_{film} (nm) ^c	ρ_{film} (eÅ ⁻³)	entry	$\sigma_{\text{film-air}}$ (nm)	T_{film} (nm) ^b	T_{film} (nm) ^c	ρ_{film} (eÅ ⁻³)
Ru ₁ -Os ₁	0.4	5.2	6.4	0.47	Ru ₂ -Os ₀	0.6	4.9	5.4	0.48	Os ₂ -Ru ₀	0.9	6.5	7.6	0.46
Ru ₂ -Os ₂	1.1	10.4	13.1	0.49	Ru ₄ -Os ₀	0.7	10.0	11.3	0.46	Os ₄ -Ru ₀	1.2	10.4	12.4	0.46
Ru ₃ -Os ₃	1.5	21.1	25.2	0.49	Ru ₄ -Os ₁	0.8	14.8	17.0	0.46	Os ₄ -Ru ₁	1.3	15.0	17.4	0.46
Ru ₄ -Os ₄	1.8	40.7	48.7	0.46	Ru ₄ -Os ₂	0.9	23.0	25.3	0.46	Os ₄ -Ru ₂	1.6	30.4	35.7	0.46
Ru ₆ -Os ₆	2.3	64.2	70.8	0.46	Ru ₄ -Os ₃	32.1	38.7	0.46	Os ₄ -Ru ₃	2.0	36.1	47.0	0.46	
					Ru ₄ -Os ₄	1.5	40.4	46.8	0.46	Os ₄ -Ru ₄	2.3	46.4	56.7	0.46

^aThe data are obtained from X-ray reflectivity (XRR) measurements and spectroscopic ellipsometry. ^bXRR-derived film thicknesses. ^cEllipsometry-derived thicknesses for the XRR samples.

varied, nearly identical film growth is expected for all SPMAs. Indeed, spectroscopic ellipsometry showed a nearly identical evolution of the thicknesses for all SPMAs (Figure S3 of the SI). For SPMAs generated by SDA I (Scheme 1, path i), the average increase of the thickness (ΔT_{nm}) does not exceed 7.0 nm per deposition step. This threshold is important as it shown that when the thickness of the ruthenium layer exceeds 8.0 nm in SDA II (Scheme 1, path ii), catalytic electron transfer was observed.⁴³ For SPMAs generated by SDA I, catalytic electron transfer is not observed, since the thickness of the ruthenium layers do not exceed this threshold. The SPMAs exhibit a regular and homogeneous distribution of the metal complexes (**1**, **2**), as shown by the linear correlation between the ¹MLCT or π - π^* bands vs thickness (Figure 2C,D). The formation of regular structures is also supported XRR measurements, which show a constant electron density as a function of the film thickness (Figure 3; vide infra).

2.3. Synchrotron X-ray Reflectivity (XRR). The XRR data demonstrate the uniformity of the SPMAs (Figure 3). A summary of the XRR-derived structural parameters are shown in Table 1. The observed Kiessig fringes in SPMAs I–III, result

from the destructive interference of reflections between substrate/film and film/air interfaces (Figure 3A–C).⁶³ The XRR-derived Patterson plots (the Fourier Transform of R/R_F)⁶⁴ for SPMA I | Ru₆-Os₆, SPMA II | Ru₄-Os₄, and SPMA III | Os₄-Ru₄ are shown in Figures S5–S7 of the SI. For SPMA I | Ru₆-Os₆ and SPMA II | Ru₄-Os₄, fluctuations in the Patterson plots were observed, with secondary local maxima at thicknesses that appear to correspond to the number of deposition steps (Figures S4 and S5 of the SI). The secondary local maxima indicated small variations of the electron density inside these SPMAs. The Pd salt that interconnects the metal complexes **1** and **2** might cause minor structural perturbations, which result in some nonuniformity of the electron density profiles. These effects are minor in the Patterson plots because the Pd interconnections are small compared with the Os or Ru complexes. Therefore, the secondary maxima and the corresponding variation in the electron density might not always be observable. For instance, for SPMA III | Os₄-Ru₄, the Patterson plot shows a smooth interface, except for a local maxima at 1.4 nm, which correlates to the template layer (Figure S6 of the SI).

Table 2. X-ray Photoelectron Spectroscopy (XPS) Derived Elemental Ratios of SPMA I | Ru₄-Os₄, SPMA II | Ru₄-Os₄, and SPMA III | Os₄-Ru₄, at Various Stages of the Assembly Formation (Scheme 1)^a

SPMA I					SPMA II					SPMA III							
entry	Pd/N ^b	Pd/M ^b	N/M ^b	Os ^c	Ru ^c	entry	Pd/N ^b	Pd/M ^b	N/M ^b	Os ^c	Ru ^c	entry	Pd/N ^b	Pd/M ^b	N/M ^b	Os ^c	Ru ^c
Ru ₁ -Os ₁	0.21	2.0	9.4	0.4	0.3	Ru ₂ -Os ₀	0.22	1.3	6.0		0.9	Os ₂ -Ru ₀	0.18	2.0	11.6	0.7	
Ru ₂ -Os ₂	0.25	2.4	9.7	0.6	0.3	Ru ₄ -Os ₀	0.17	1.6	9.0		0.9	Os ₄ -Ru ₀	0.18	2.0	10.9	0.8	
Ru ₃ -Os ₃	0.20	2.5	12.5	0.8		Ru ₄ -Os ₁	0.17	1.7	9.6	0.7	0.2	Os ₄ -Ru ₁	0.16	1	6	0.1	1.3
Ru ₄ -Os ₄	0.20	1.5	7.8	1.1		Ru ₄ -Os ₂	0.18	2.0	11.2	0.8		Os ₄ -Ru ₂	0.18	1.1	5.9	0.1	1.3
						Ru ₄ -Os ₄	0.18	1.6	8.6	0.8		Os ₄ -Ru ₄	0.18	1.2	6.4	0.1	1.3

^aThe XPS spectra were recorded at a take-off angle of $\theta = 45^\circ$. For a more extensive overview of the atomic concentrations for selected samples at various take-off angles see Tables S1, S2, and S3 of the SI. ^bXPS derived elemental ratios, where M = Os and Ru. ^cAtomic concentration of Os or Ru.

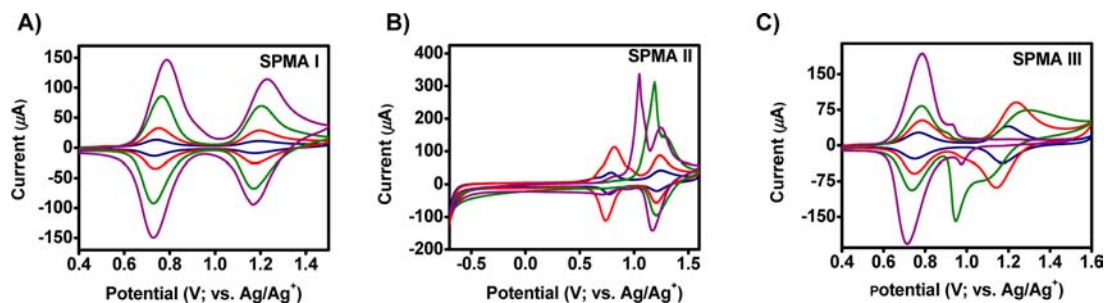


Figure 4. Cyclic voltammograms (CVs) of self-propagating molecular assemblies (SPMAs), on ITO, at various thicknesses. (A) CVs at 100 mV s⁻¹ of SPMA I | Ru₁-Os₁ (blue trace), SPMA I | Ru₂-Os₂ (red trace), SPMA I | Ru₃-Os₃ (green trace), and SPMA I | Ru₄-Os₄ (purple trace), with thicknesses of 5.4, 11.4, 23.8, and 36.7 nm, respectively. (B) CVs at 200 mV s⁻¹ of SPMA II | Ru₁-Os₁ (blue trace), SPMA II | Ru₂-Os₂ (red trace), SPMA II | Ru₃-Os₃ (green trace), and SPMA II | Ru₄-Os₄ (purple trace), with thicknesses of 5.8, 12.4, 25.6, and 43.6 nm, respectively. (C) CVs at 200 mV s⁻¹ of SPMA III | Os₁-Ru₁ (blue trace), SPMA III | Os₂-Ru₂ (red trace), SPMA III | Os₃-Ru₃ (green trace), and SPMA III | Os₄-Ru₄ (purple trace), with thicknesses of 3.8, 8.7, 15.7, and 38.9 nm respectively. The SPMAs were constructed according to SDA I (A), SDA II (B), or SDA III (C).

However, due to negligible changes in electron density between osmium and ruthenium layers, the small fluctuations in the Patterson functions—which usually indicate slight non-uniformity of the electron density profiles inside the SPMAs—are not reflected in the electron density profiles (Figure 3D–F). Indeed, the XRR-derived electron density profiles do not vary significantly as a function of the film thickness, and the resulting SPMAs have an average electron density of a $\rho = 0.46 \text{ e}\text{\AA}^{-3}$ (Table 1). The similarity of the electron density of each layer is indicative of a homogeneous superlattice. Such a homogeneous superlattice was also confirmed by the optical data (vide supra), which showed that the molecular density (ρ) is constant, and does not vary significantly for SPMAs formed with SDA I–III (Figure 2C,D). The identical coordination chemistry of the metal complexes (1, 2), allows for maximum interaction between the two types of metal complexes, resulting in a continuous growth (Figures 1 and 2) and formation of homogeneous assemblies.

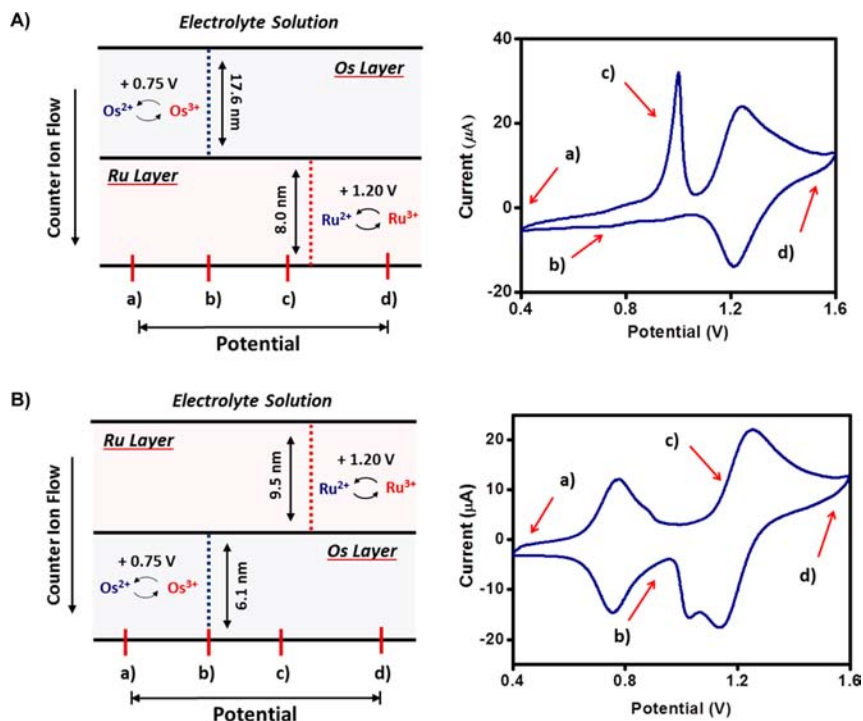
The XRR-derived thickness corresponds well with those derived from spectroscopic ellipsometry, and demonstrates and exponential growth behavior. (Figure S7 of the SI). The surface roughness for all SPMAs varies between 5 and 10% of the film thickness. For instance, SPMAs with a film thickness of ~ 40 nm display a surface roughness between 1.5 and 2.2 nm (Table 1). These values are comparable to previously reported values of SPMAs constructed with metal complex 2.¹⁵ The XRR data thus indicate the formation of homogeneous assemblies, with nearly constant electron densities with little variation among the SPMAs.

2.4. X-ray Photoelectron Spectroscopy (XPS). The internal composition of the SPMAs was analyzed by AR-XPS.⁶⁷ For fully formed networks, with two pyridine groups

coordinated to a palladium center, the following ratios are expected: Pd/N = 0.17; Pd/M = 1.5; and N/M = 9 (M = Os or Ru).¹⁵ For all SPMAs, the XPS-derived elemental ratios are close to their expected values. However, the palladium content is slightly higher than their predicted theoretical values. An higher palladium content is not uncommon, since our SPMAs are able to store excess palladium inside their porous network.¹⁵ The ratios for SPMA I | Ru₄-Os₄, SPMA II | Ru₄-Os₄, and SPMA III | Os₄-Ru₄, are summarized in Table 2.

For SPMAs I and II, significant atomic concentrations of ruthenium (1) are observed, although the film is terminated with a layer of the osmium complex 2 (Table 2). For example, in SPMA I, higher ruthenium concentrations are observed for entry Ru₁-Os₁ (5.4 nm) and Ru₂-Os₂ (11.4 nm), where the thickness of the combined osmium layers is 1.5 and 3.2 nm respectively. In SPMA II for entry Ru₄-Os₁ (15.5 nm) the underlying ruthenium layer is observed as well, after a deposition of a 5.0 nm thick osmium layer. This effect might be a result of the XPS probe depth of ~ 6.0 nm at a 45° takeoff angle.⁶⁸ Alternatively, the pronounced presence of the ruthenium can be explained by some Ru/Os intermixing at the internal interfaces of the SPMA.

For higher thicknesses in SPMA I, only one of the metals is observed; entry Ru₃-Os₃ (23.8 nm) and Ru₄-Os₄ (36.7 nm), depending on which metal complex was deposited last. These results indicate that clear and distinct layers are being formed inside the SPMA that are composed of only one type of metal complex. The same effects are observed for SPMA II and III (Table 2). This layering is a direct result of the SDA and is responsible for the spectroelectrochemical properties as discussed below.

Scheme 2. Electron Transfer in Self-Propagating Molecular Assemblies (SPMAs) Constructed According to SDA II or III^a

^a(A) Oxidative catalytic electron transfer in SPMA II | Ru₃-Os₃ (25 mV s⁻¹) at potentials of 0.40 V (a) or 1.60 V (d) the SPMAs are entirely reduced or oxidized, respectively. At an intermediate potential of 1.00 V (c) small amounts of Ru²⁺ are oxidized to Ru³⁺. Since the Ru³⁺ is able to oxidize Os²⁺ a sharp increase in the current is observed in which the ruthenium layer act as a catalytic gate for the oxidation of the osmium layer. However, at the half-wave potential (0.75 V) of the Os^{2+/3+} redox-couple (b), no oxidation/reduction is observed due to the insulating nature of the 8.0 nm thick ruthenium layer and charge trapping occurs. (B). Reductive catalytic electron transfer in SPMA III | Os₃-Ru₃ (25 mV s⁻¹). At potentials of 0.40 V (a) or 1.60 V (d) the SPMAs are entirely reduced or oxidized, respectively. At intermediated potentials, the electron has two possibilities in reaching the outer ruthenium layer: (i) at 1.20 V (c) the electron transfer is reversible but hampered by the osmium layer and (ii) at 1.00 V (b) a catalytic transfer is observed due oxidation of the newly formed Os²⁺ metal centers by the remaining Ru³⁺ centers.

2.5. Electrochemistry. The SDA-dependent physicochemical properties (e.g., film thickness, interface formation) are expressed in the electrochemical properties of the SPMAs. For SDA I, the electron transfer is reversible for SPMA I at various thicknesses (Figure 4A). The single oxidation/reduction waves observed in the CV indicate that the Os and Ru centers have the same or a very similar chemical environment (Figure 4). In the seminal work of Balzani et al., about dendritic systems in solution, it was shown that the oxidation of the metal centers in the periphery changed the oxidation potential of the metal centers in the core.⁶⁹⁻⁷¹ Such changes in the oxidation/reduction potentials are absent for SPMA I and for SPMA II/III below their respective threshold thicknesses (SPMA II: 8.0 nm and SPMA III: 6.0 nm). For thicker assemblies, the metal-metal communication becomes important for the overall electron transfer, although the nature of the electron transfer is inherently different than for dendritic systems (vide infra).

The thickness of the layers of metal complexes (1, 2), contributes to the observed reversible behavior. For SDA II similar behavior is observed for SPMA II | Ru₁-Os₁ (5.8 nm; blue trace) and SPMA II | Ru₂-Os₂ (12.4 nm; red trace), since for these SPMAs, the thickness of the ruthenium layer is below the threshold value of 8.0 nm (Figure 4B). However, for SPMA II | Ru₃-Os₃ (25.6 nm; green trace), and SPMA II | Ru₄-Os₄ (43.6 nm; purple trace), the thickness of the ruthenium layer exceeds 8.0 nm and a catalytic prewave is observed. Such catalytic prewaves were first observed in the seminal work of Murray et al. on polymeric films of metal complexes.⁷²⁻⁷⁴ In

addition, unidirectional current flows have also been observed with functionalized electrodes and ferrocyanide solutions or surface confined ionic polymers.⁷⁵⁻⁸¹ Accordingly, the oxidative catalytic behavior above an 8.0 nm thickness of the ruthenium layer can be illustrated as follows (Scheme 2A): At a potential of 0.4 V, (a) the entire SPMA is reduced. Next, the potential bias is increased to the half-wave potential (0.75 V) of the Os^{2+/3+} redox-couple (b). No oxidation is observed due to the insulating nature of the 8.0 nm thick ruthenium layer. However, when the potential reaches the onset-potential (1.0 V) of the ruthenium oxidation (c), small amounts of Ru²⁺ are oxidized to Ru³⁺. Since the Ru³⁺ is able to oxidize Os²⁺, a sharp increase in the current is observed in which the ruthenium layer acts as a catalytic gate for the oxidation of the osmium layer. Finally, when a potential of 1.60 V is reached (d), the entire SPMA is oxidized. However, when the potential is reversed, charge-trapping occurs. At 1.00 V (c), the entire ruthenium layer is reduced, therefore, when the half-wave potential of the Os^{2+/3+} redox-couple is reached (b), the electron transfer from the electrode to the osmium layer is blocked. Consequently, the second scan cycle in the CV always shows a diminished height of the catalytic prewave, due to the charge trapping (Figure S8 of the SI).

For SDA III, the opposite behavior is observed, since the thermodynamic driving force of the electrochemical potential is now reversed. This effect is most pronounced in SPMA III | Os₄-Ru₄ (Figure 4; purple trace), with a thickness of the osmium layer of 11.0 nm. At these thicknesses, the ruthenium

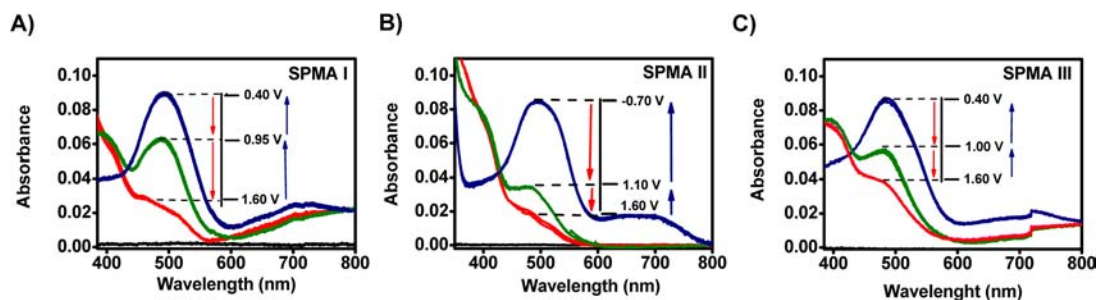


Figure 5. Optical absorption of SPMA formed according SDAs I–III (Scheme 1), after applying various potential biases. (A) UV–vis spectra of SPMA I | Ru₄–Os₃, after applying a potential bias of 0.40 V (blue), 0.95 V (green trace), and 1.60 V (red trace) for 60 s. (B) UV–vis spectra of SPMA II | Ru₃–Os₃, after applying a potential bias of –0.70 V (blue trace), 1.10 V (green trace), and 1.60 V (red trace) for 60 s. (C) UV–vis spectra of SPMA III | Os₃–Ru₃, after applying a potential bias of 0.40 V (blue trace), 1.00 V (green trace), and 1.60 V (red trace) for 60 s. The black trace represents the baseline.

complexes are isolated from the ITO-electrode (Figure 4C; purple trace). For SPMA III | Os₁–Ru₁ (Figure 4; blue trace) in contrast, both metal complexes display reversible behavior. The catalytic electron transfer is only observed for SPMA III | Os₂–Ru₂ (Figure 4; red trace), and SPMA III | Os₃–Ru₃ (Figure 4; green trace). Since the distribution of the electrochemical potentials is reversed in SDA III, compared to SDA II, the catalytic prewave arises differently. According to the same principles as outlined by Murray et al. for polymeric systems;^{72–74} this catalytic reductive prewave is explained as follows (Scheme 2B): Upon increasing the potential to 1.6 V (d), the oxidation of the outer ruthenium layer is severely hampered by the presence of the osmium layer (3.0–5.0 nm), indicated by the large peak to peak separation ($\Delta E_p = 200$ mV). Although hampered, the oxidation of the ruthenium layer still occurs. When reversing the potential, and scanning in the negative scanning direction, at 1.20 V (c), the reduction of the ruthenium layer occurs although this is difficult, hence the large peak to peak separation (vide supra). Therefore, at the onset potential (1.00 V) the Os³⁺ metal centers are being reduced to Os²⁺ (b). Since the outer ruthenium layer is not yet fully reduced, the remaining Ru³⁺ centers immediately oxidize the newly formed Os²⁺ metal centers. As a result, a reductive catalytic prewave at 1.00 V appears, in which the electron is transferred from the ITO electrode to the outer ruthenium layer, mediated by the osmium layer. At 0.40 V (a) the SPMA is completely reduced and charge trapping only occurs, between 1.00 and 1.20 V. Therefore, depending on the thickness of the osmium layer, the electron has two possibilities of reaching the outer ruthenium layer: (i) without or (ii) with the osmium metal centers as mediator. This might explain why the equilibrium between reversible electron transfer and catalytic electron transfer in SPMA III | Os₃–Ru₃ (Figure 4; green trace) changes as a function of the scan rate. Unlike SDA II, where the oxidation of the Os²⁺ metal centers occurs irrespective of the thickness of the ruthenium layer. For SDA III, the oxidation of the Ru²⁺ metal centers is dependent on the thickness of the osmium layer. Only when the thickness of the osmium layer exceeds 11.0 nm, the electron transfer is completely blocked and no electrochemical signal of the ruthenium is observed (Figure 4C; purple trace).

2.6. Spectroelectrochemistry. The different electrochemical behavior among the SPMA, formed with the different SDAs I–III, is also expressed in their spectroelectrochemical properties. Figure 5 shows the optical absorption spectra between 400 and 800 nm of SPMA I | Ru₄–Os₃, SPMA II | Ru₃–Os₃, and SPMA III | Os₃–Ru₃. Three distinct absorption

values can be obtained upon applying three different potential biases. At a potential of 0.40 V both Ru and Os metal centers are fully reduced and the ¹MLCT at $\lambda = 495$ shows an intense absorption (Figure 5; blue traces—State I: Os²⁺|Ru²⁺). However, for SPMA II | Ru₃–Os₃, a negative potential (–0.70 V) was needed to fully reduce the SPMA and overcome the charge trapping (Figure 5B).

When holding the potential between 0.95 and 1.10 V, all the osmium complexes (2) of the assembly are oxidized, while the Ru-based components are still in their reduced state (Figure 5; green trace—State II: Os³⁺|Ru²⁺). The oxidation of the Os metal centers is indicated by a concurrent decrease of both the ¹MLCT and ³MLCT bands at $\lambda = 495$ and 700 nm, respectively. Full oxidation of the SPMA, as indicated by full bleaching of the ¹MLCT band, is accomplished by applying a potential of 1.60 V (Figure 5; red trace—State III: Os³⁺|Ru³⁺). This oxidation is incomplete for SPMA III | Os₃–Ru₃, as shown by the unusual high remaining absorption of the ¹MLCT band (Figure 5C; red trace). Discrimination between the Os^{2+/3+}- and Ru^{2+/3+}-based redox processes is optically possible since the Ru-based complex 1 lacks a ³MLCT band at $\lambda \approx 700$ nm.^{55,56} As a consequence, a decrease of the ³MLCT band is only observed when a potential of 0.95–1.10 V (Os²⁺ → Os³⁺) is applied, whereas such a decrease is absent when a potential of 1.60 V (Ru²⁺ → Ru³⁺) is used (Figure 5).

In order to further investigate the oxidation/reduction of the individual type of metal complexes; i.e., ruthenium (1) or osmium (2), SPMA constructed according to SDA I were selected. These SPMA are preferable since there is no interference by catalytic electron transfer, as is the case in SDA II and III. In order to assess the electrochromic properties in detail, the optical response of SPMA I | Ru₅–Os₄ was measured as a function of the potential. For instance, gradually increasing the switching potential between 0.5 and 0.5 + $n \times 0.05$ V, with $n = 0–22$, in the chronoamperometric mode, results clearly in a double-step sigmoidal shape associated with the characteristic electrochemical properties of the Ru^{2+/3+} and Os^{2+/3+} redox-couples (Figure 6A). Differentiation of the sigmoidal fit produces a normal distribution centered on the $E_{1/2}$ of the ruthenium (1) and osmium (2) complexes (Figure 6B), and demonstrates that there is no overlap in the oxidation of the individual type of metal complexes.^{82,83} This confirms that no metal–metal communication occurs in SPMA created by SDA I, in contrast to SPMA formed by SDA II and III.

The optical response of the ¹MLCT at $\lambda = 495$ nm for SDA I, II, and III was further used to read-out the electronic

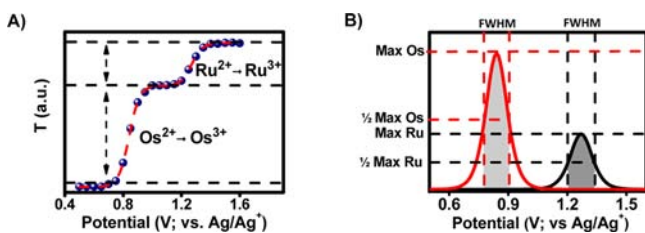


Figure 6. (A) Optical transmission of the metal-to-ligand charge-transfer ($^1\text{MLCT}$) band, at $\lambda = 495$ nm, of a SPMA I | $\text{Ru}_5\text{-Os}_4$ (49 nm), as a function of the voltage. The dashed red line is a sigmoidal fit ($R^2 = 0.99$), with inflection points at 0.84 V ($\text{Os}^{2+/3+}$) and at 1.27 V ($\text{Ru}^{2+/3+}$) that corresponds to the half-wave potentials of complexes 1 and 2 in the SPMA. (B) Derivative of the sigmoidal fit and the resulting full-width at half-maximum (fwhm).

properties of the SPMA by applying short potential biases. For instance, for SDA I the optical response of the $^1\text{MLCT}$ of SPMA I | $\text{Ru}_4\text{-Os}_3$ is shown in Figure 7. The blue trace in

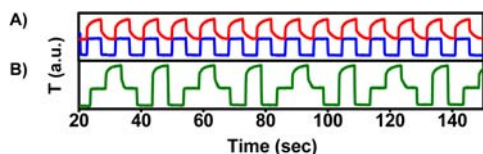


Figure 7. Spectroelectrochemistry of SPMA I | $\text{Ru}_4\text{-Os}_3$ formed by SDA I (Scheme 1). Optical transmission (T) of the $^1\text{MLCT}$ band at $\lambda = 495$ nm, with a thickness of the SPMA of 29.3 nm, upon (A) applying double potential steps between 0.40–0.95 V (blue traces) and between 0.95–1.60 V (red traces), or (B) upon applying triple potential steps between 0.40, 0.95, and 1.60 V, followed by double potential steps between 0.4–1.60 V (green traces).

Figure 7A shows the switching of the Os metal centers upon applying a double potential step between 0.40 and 0.95 V. It was observed that the switching from $\text{Os}^{2+} \rightarrow \text{Os}^{3+}$ is more efficient, than the oxidation from $\text{Ru}^{2+} \rightarrow \text{Ru}^{3+}$ (Figure 7A; red trace). The difference between the osmium (0.77 V) and ruthenium (1.20 V) oxidation is evident from the gradual increase of the optical response until full oxidation of the SPMA occurs, after applying a double potential step between 0.95 and 1.60 V. The gradual oxidation at higher thicknesses is due to the more distant ruthenium centers, with respect to the ITO surface, that are more difficult to oxidize. This effect was not observed for thinner SPMA (e.g., 11.4 nm) where the oxidation of the ruthenium is nearly instantaneous upon applying the both double potential steps (Figure S9 of the SI). Applying triple potential steps between 0.40, 0.95, and 1.60 V resulted in three clearly distinguishable absorption states (Figure 7B). Therefore, applying the different potential biases effectively modulates the SPMA among its three different oxidation states; State 1; $\text{Os}^{2+}|\text{Ru}^{2+}$, State 2; $\text{Os}^{3+}|\text{Ru}^{2+}$, and State 3; $\text{Os}^{3+}|\text{Ru}^{3+}$.⁸⁴ It is important to realize that the three different absorption states are not the result of the SPMA as a whole, but rather from the individual type of metal complexes (1; Ru and 2; Os), that constitutes the individual layers in the SPMA. Therefore, these systems are ideal candidates for applications in electrochromic surfaces or memory devices where the information density has increased from binary to ternary.^{82,83}

The difference between reversible and unidirectional current flow in SDA II is also manifested in the spectroelectrochemical behavior of the SPMA. For SPMA with a thickness of the

ruthenium layer of 5.7 nm and a thickness of the osmium layer of 6.8 nm (SPMA II | $\text{Ru}_2\text{-Os}_2$), reversible behavior in the electro-optical properties was observed. Applying potential biases of 0.40, 1.00, and 1.60 V for 5 s (Figure 8A; red trace),

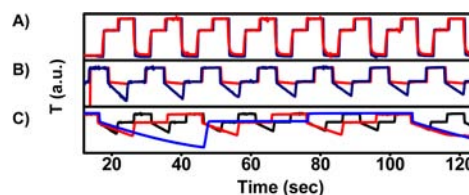


Figure 8. Spectroelectrochemistry of self-propagating molecular assemblies (SPMA) formed by SDA II (Scheme 1). Optical transmission of the $^1\text{MLCT}$ at $\lambda = 495$ nm of SPMA with (A) a thickness of the ruthenium layer of 5.7 nm and a thickness of the osmium layer of 6.8 nm (SPMA II | $\text{Ru}_2\text{-Os}_2$) and with (B) a thickness of the ruthenium layer of 8.0 nm and a thickness of the osmium layer of 17.6 nm (SPMA II | $\text{Ru}_3\text{-Os}_3$) as a function of time upon applying triple-potential steps (5 s) between 0.40, 1.00, and 1.60 V (red traces) or applying triple potential steps (5 s) between -0.70 , 1.10, and 1.60 V (blue traces). Part (C) shows the time dependence of the reduction of the osmium content in an SPMA with a thickness of the ruthenium layer of 8.0 nm and a thickness of the osmium layer of 17.6 nm (SPMA II | $\text{Ru}_3\text{-Os}_3$), upon applying triple-potential steps between -0.70 , 1.10, and 1.60 V for 5 s (black traces), 10 s (red traces) and 30 s (blue traces).

shows that both metal centers 1 and 2 can be modulated reversibly between the oxidation states ($\text{M}^{2+/3+}$). Changing the potentials to -0.70 , 1.10, and 1.60 V does not alter this behavior, and is in accordance with the CV experiments (Figure 8A; black trace). However, the spectroelectrochemical behavior is strikingly different for SPMA with a thickness of the ruthenium layer of 8.0 nm and a thickness of the osmium layer of 17.6 nm (SPMA II | $\text{Ru}_3\text{-Os}_3$). When potential biases of 0.40, 1.00, and 1.60 V are applied for 5 s. (Figure 8B; red trace), the osmium in the SPMA can only be oxidized once. Thereafter, applying a potential of 0.40 V does not lead to reduction of the osmium centers. We expect the reduction to occur because the potential is 0.37 V below the $E_{1/2}$ of $\text{Os}^{2+/3+}$ redox couple (0.77 V; vs Ag/Ag^+). The charge trapping of the Os^{3+} metal centers is evident in the spectroelectrochemical properties of SPMA II | $\text{Ru}_3\text{-Os}_3$. The absence of reversible oxidation/reduction processes for the $\text{Os}^{2+/3+}$ redox couple upon applying 0.40 or 1.00 V is illustrated by the flat red line in Figure 8B. Note that the oxidation/reduction of the $\text{Ru}^{2+/3+}$ redox couple in this SPMA is reversible. When the potential biases are changed to -0.70 and 1.10 V, oxidation and reduction are observed for the $\text{Os}^{2+/3+}$ redox couple (Figure 8B; blue trace). Although oxidation of the Os metal centers is now instant—mediated by the Ru^{2+} layer reduction—remains difficult to achieve, even at a potential that is 1.00 V below the $E_{1/2}$ of the $\text{Os}^{2+/3+}$ redox couple. Due to the insulating nature of the 8.0 nm thick Ru^{2+} layer, a further increase in the Os^{2+} content is only observed upon applying a potential biases of -0.70 V for 5 s (Figure 8C; black trace), 10 s (Figure 8C; red trace), and 30 s (Figure 8C; blue trace). Further increasing the thickness of the ruthenium layer to 10.7 nm (SPMA II | $\text{Ru}_4\text{-Os}_4$) does not alter the catalytic prewave (Figure 4B; purple trace) in the CV nor does it change the spectroelectrochemical properties (Figure S10 of the SI) compared to SPMA II | $\text{Ru}_3\text{-Os}_3$. It is captivating that by solely increasing the thickness of the ruthenium layer from 5.7 to 8.0 nm

significant differences in the spectroelectrochemical behavior are evident.

The spectroelectrochemical properties of SPMAs constructed according to SDA III are presented in Figure 9. For

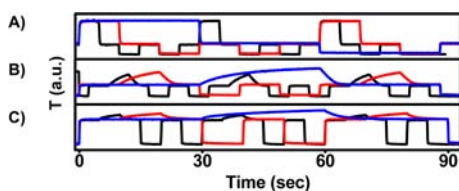


Figure 9. Spectroelectrochemistry of self-propagating molecular assemblies (SPMA) formed by SDA III (Scheme 1). Optical transmission of ¹MLCT at $\lambda = 495$ nm of SPMA (A) with a thickness of the osmium layer of 3.8 nm and a thickness of the ruthenium layer of 5.0 nm (SPMA III | Os₂-Ru₂), (B) with a thickness of the osmium layer of 6.1 nm and a thickness of the ruthenium layer of 9.5 nm (SPMA III | Os₃-Ru₃), and (C) with a thickness of the osmium layer of 11.0 nm and a thickness of the ruthenium layer of 27.8 nm (SPMA III | Os₄-Ru₄), upon applying triple-potential steps at intervals of -0.70, 1.10, and 1.60 V for 5 s (black traces), 10 s (red traces), and 30 s (blue traces).

SPMA with a maximum thickness of the osmium layer of ~3.8 nm, the spectroelectrochemical behavior exhibits reversible behavior. This reversible behavior illustrated by SPMA III | Os₂-Ru₂, where three clear states are observed after applying potential biases at of 0.40, 1.00, and 1.60 V, which correspond to the three different oxidation states of the SPMA (Figure 9A). Increasing the duration of the potential biases from 5 s (Figure

9A; black trace), to 10 s (Figure 9A; red trace), and 30 s (Figure 9A blue trace), does not lead to an increase/decrease in the optical absorption of the interfaces indicating immediate oxidation of the SPMA upon applying the potential bias. This reversibility is independent of the thickness of the outer ruthenium layer, formed by complex 1. Although, the CV of SPMA III | Os₂-Ru₂ shows the evolution of a reductive catalytic prewave at higher scan rates (300–700 mV/s; Figure S11 of the SI), it did not affect the reversibility of the oxidation/reduction of the ruthenium redox couple.

The effect of the reductive catalytic prewave only becomes apparent in the spectroelectrochemical properties upon increasing the thickness of the osmium layer to 6.1 nm (SPMA III | Os₃-Ru₃). At this thickness, the insulating nature of the osmium layer becomes apparent, so oxidation of the Ru metal centers is retarded. This hampered oxidation is clearly visible optically, since the transmission slowly increases upon applying a potential bias of 1.6 V (Figure 9B). Increasing the duration of the bias to 10 and 30 s shows that the oxidation is time dependent, as is evident from the increase in the content of the Ru³⁺ metal centers in the SPMA (Figure 9B; red and blue traces). Further increasing the thickness of the osmium layer to 11.0 nm (SPMA III | Os₄-Ru₄) did not result in any oxidation or reduction of ruthenium in the CV (Figure 4C; purple trace). However, some oxidation does occur after prolonged exposure of the SPMA to a potential bias, judging from the small increase in the transmission after applying the potential (1.60 V) for 5 s (Figure 9C; black trace), 10 s (Figure 9C; red trace), and 30 s (Figure 9C; blue trace). The above-mentioned results unequivocally demonstrate that the observed

Table 3. Summary of the SPMA Formed by SDA II and III, for Which (Green Checkmark), or for Which Not (Red X), a Catalytic Pre-Wave Was Observed, Depending on the Thickness of the Initial Ruthenium (1) or Osmium (2) Layer, and the Subsequent Number of Deposition Steps of Complexes 1 and 2

SDA II				SDA III			
Ru Thickness	SPMA II	Oxidative Catalytic Pre-wave		Os Thickness	SPMA III	Reductive Catalytic Pre-wave	
		No	Yes			No	Yes
3.3 nm	Ru ₁ -Os ₀	✗		2.6 nm	Os ₁ -Ru ₀	✗	
	Ru ₁ -Os ₁	✗			Os ₁ -Ru ₁	✗	
	Ru ₂ -Os ₀	✗			Os ₂ -Ru ₀	✗	✓
5.7 nm	Ru ₂ -Os ₁	✗		3.8 nm ^a	Os ₂ -Ru ₁	✗	✓
	Ru ₂ -Os ₂	✗			Os ₂ -Ru ₂	✗	✓
	Ru ₃ -Os ₀	✗			Os ₃ -Ru ₀	✗	
8.0 nm	Ru ₃ -Os ₁		✓	6.1 nm	Os ₃ -Ru ₁		✓
	Ru ₃ -Os ₂		✓		Os ₃ -Ru ₂		✓
	Ru ₃ -Os ₃		✓		Os ₃ -Ru ₃		✓
10.6 nm	Ru ₄ -Os ₀	✗		11.0 nm	Os ₄ -Ru ₀	✗	
	Ru ₄ -Os ₁		✓		Os ₄ -Ru ₁	✗	
	Ru ₄ -Os ₂		✓		Os ₄ -Ru ₂	✗	
	Ru ₄ -Os ₃		✓		Os ₄ -Ru ₃	✗	
	Ru ₄ -Os ₄		✓		Os ₄ -Ru ₄	✗	

^a The appearance of the reductive pre-wave depends on the scan rate. Only for scan rate > 300 mV s⁻¹, the catalytic reductive pre-waves are clearly observed (Figure S11).

metal-mediated electron transfer has significant effects on the electrochemical and spectroelectrochemical properties. These properties are not only a function of the assembly sequence, but are also dependent on the thickness of the ruthenium/osmium layers, an overview of which SPMA demonstrates an oxidative/reductive prewave, depending on the thickness of the ruthenium (1) and osmium (2) thickness is given in Table 3, and highlights the importance of SDA.

3. CONCLUSIONS

Three different SPMA were obtained according to the SDA shown in Scheme 1. All of the SPMA displayed an exponential growth in their film thickness and in the optical properties of the π - π^* and MLCT bands. Even though the three SPMA were formed using different SDAs, their optical and structural properties are nearly identical. XRR analysis of the SPMA revealed a similar electron density and surface roughness. The main difference between the SPMA is in the internal composition, e.g., the distribution of the osmium and ruthenium complexes 1 and 2. The SPMA demonstrate homogeneous interfaces that consist only of one type of metal complex. The formation of these interfaces is a direct result of SDA in combination with a high stability of the metal complexes (no lateral diffusion upon incorporation) and a low surface roughness. Only at the Os/Ru or Ru/Os interface, some intermixing of the metal complexes might occur. For an alternating assembly sequence (SDA I), XPS revealed alternating interfaces of osmium and ruthenium, according to the assembly sequence. Since for SDA I, the individual layers do not exceed the threshold thickness of 8.0 nm, reversible electrochemical behavior is observed for both metal complexes. The well-separated oxidation potentials of the ruthenium and osmium polypyridyl complexes 1 and 2 allow for individual addressing of both types of metal centers, which is beneficial for multistate memory.^{82,83} For SDA II and III, this is not the case due to communication among the complexes. XPS analysis showed two distinct layers containing either osmium or ruthenium. The presence of a sufficiently thick initial layer of ruthenium (8.0 nm) or osmium (6.0 nm) results in catalytic electron transfer.

The profound changes in the electrochemistry and spectroelectrochemistry upon changing the thickness of ruthenium and osmium layers, together with the applied SDA highlights the importance of this work (Table 3). These obtained results unequivocally demonstrated that the sequence in which molecular components are assembled can have important consequences for the material properties or other emerging systems where SDA is of critical importance.^{85–87}

4. EXPERIMENTAL SECTION

4.1. General Procedures. The synthesis of complexes 1, 2, and 1,3,5-tris(4-ethenylpyridyl)benzene (3) were prepared according to literature procedures.^{15,61,88,89} *Trans*-Pd(PhCN)₂Cl₂ was used for assembly formation. The silicon, quartz, and ITO substrates were cleaned according to standard procedures outlined elsewhere.¹⁵ Modification of these surfaces by siloxane-based chemistry and the formation of the 3-based template layer were carried out in a glovebox or by using standard Schlenk-cannula techniques.^{49,89,90} The freshly prepared 3-based template layers were used for formation of the SPMA I–III according to the SDA outlined in Scheme 1.⁴¹ The UV–vis spectra were recorded on a Cary 100 spectrophotometer. Spectroscopic ellipsometry was recorded on an M 2000 V (J. A. Wollam Co. Inc.) instrument with VASE32 software. The thicknesses of the SPMA on ITO were estimated by spectroscopic ellipsometry

measurements of SPMA grown simultaneously on silicon substrates. One deposition step is defined as the deposition of one type of metal complex (1 or 2) and the palladium salt *trans*-Pd(PhCN)₂Cl₂. All experiments were carried out at room temperature, unless stated otherwise.

4.2. X-ray Reflectivity (XRR). Synchrotron XRR studies were performed at beamline X6B of the National Synchrotron Light Source (NSLS; Brookhaven National Laboratory, U.S.), using a Huber four-circle diffractometer in the specular reflection mode (i.e., the incident angle is equal to the exit angle θ). The reflected intensity was measured as a function of the scattering vector component $q_z = (4\pi/\lambda) \sin \theta$, perpendicular to the reflecting surface. X-rays of energy $E = 10$ keV ($\lambda = 1.240$ Å) were used with a beam size of 0.3 mm vertically and 0.5 mm horizontally. The resolution was 3×10^{-3} Å⁻¹. The samples were placed under a slight overpressure of helium during the measurements to reduce the background scattering from the ambient gas and radiation damage. The off-specular background was measured and subtracted from the specular counts. Details of the data acquisition and analysis are given elsewhere.^{65,66} The XRR measurements were performed at 20–25 °C.

4.3. X-ray Photoelectron Spectroscopy (XPS). Angle-resolved X-ray photoelectron spectra (AR-XPS) were made at different takeoff angles with a PHI 5600 Multi Technique System (base pressure of the main chamber 2×10^{-10} Torr). Resolution, corrections for satellite contributions, procedures to account for steady-state charging effects, and background removal have been described elsewhere. Experimental uncertainty in binding energies lies within ± 0.4 eV.

4.4. Electrochemical Measurements. Cyclic voltammetry and chronoamperometry were performed in a three-electrode cell configuration on a CHI 660A potentiostat. ITO electrodes functionalized with our SPMA were used as the working electrode, whereas Pt- and Ag-wires were used as counter and reference electrodes, respectively. Solutions of Bu₄NPF₆ (0.1 M) in dry acetonitrile were used as the electrolyte. The Fc/Fc⁺ redox-couple, used as an internal standard, was set at 0.40 V vs SCE under these conditions.⁹¹ All electrochemical measurements were performed at RT in air.

4.5. Spectroelectrochemistry. Spectroelectrochemical measurements were performed in a 3 mL quartz cuvette fitted in a Varian Cary 100 spectrophotometer operating in the double-beam transmission mode (200–800 nm). The potential was modulated with a CHI 660 A potentiostat operating in a three-electrode cell configuration consisting of (i) an SPMA-functionalized ITO substrate as the working electrode, (ii) a Pt wire as the counter electrode, and (iii) an Ag-wire as the reference electrode. Dry propylene carbonate containing 0.1 M Bu₄NPF₆ was used as the electrolyte solution. The UV–vis spectra were recorded in the dark, as soon as the electrochemical potential was applied. All spectroelectrochemical measurements were performed in the chronoamperometry mode at RT.

■ ASSOCIATED CONTENT

Supporting Information

Optical absorption spectra of SPMA; absorption intensity of the ³MLCT band; spectroscopically derived thicknesses of SPMA; XRR-derived Patterson plots and thicknesses; XPS derived atomic concentrations; and CVs and spectroelectrochemistries of various compounds (Figures S1–S11 and Tables S1–S5); along with additional references. This material is available free of charge via the Internet at <http://pubs.acs.org>.

■ AUTHOR INFORMATION

Corresponding Author

milko.vanderboom@weizmann.ac.il

Notes

The authors declare no competing financial interest.

■ ACKNOWLEDGMENTS

This research was supported by the Helen and Martin Kimmel Center for Molecular Design, Mary and Tom Beck-Canadian Center for Alternative Energy Research, David Rosenberg (Chicago, IL), the Yeda-Sela Center for Basic Research, a research grant from the Leona M. and the Harry B. Helmsley Charitable Trust, and by the U.S. National Science Foundation under Grant No. DMR-1309589. G.E. acknowledges support from the Center for Electrical Energy Storage, an Energy Frontier Research Center funded by DOE (award number DE-AC02-06CH11357). The X-ray reflectivity measurements were performed at Beamline X6B of the National Synchrotron Light Source, supported by the U.S. Department of Energy (DE-AC02-98CH10886). We would like to thank Dr. Joyanta Choudhury for his useful contributions. M.v.d.B. is the incumbent of the Bruce A. Pearlman Professorial Chair in Synthetic Organic Chemistry.

■ REFERENCES

- (1) Ribas, J. *Coordination Chemistry*; Wiley-VCH Verlag: Weinheim, Germany, 2008.
- (2) Alexeev, Y. E.; Kharisov, B. I.; Garcia, T. C. H.; Garnovskii, A. D. *Coord. Chem. Rev.* **2010**, *254*, 794.
- (3) Campbell, V. E.; de Hatten, X.; Delsuc, N.; Kauffmann, B.; Huc, I.; Nitschke, J. R. *Nat. Chem.* **2010**, *2*, 684.
- (4) de Hatten, X.; Asil, D.; Friend, R. H.; Nitschke, J. R. *J. Am. Chem. Soc.* **2012**, *134*, 19170.
- (5) Cook, T. R.; Zheng, Y. R.; Stang, P. J. *Chem. Rev.* **2009**, *113*, 734.
- (6) Northrop, B. H.; Zheng, Y. R.; Chi, K. W.; Stang, P. J. *Acc. Chem. Res.* **2009**, *42*, 1554.
- (7) Zheng, Y. R.; Zhao, Z. G.; Wang, M.; Ghosh, K.; Pollock, J. B.; Cook, T. R.; Stang, P. J. *J. Am. Chem. Soc.* **2010**, *132*, 16873.
- (8) Altman, M.; Zenkina, O.; Evmenenko, G.; Dutta, P.; van der Boom, M. E. *J. Am. Chem. Soc.* **2008**, *130*, 5040.
- (9) Doron-Mor, I.; Hatzor, A.; Vaskevich, A.; van der Boom-Moav, T.; Shanzer, A.; Rubinstein, I.; Cohen, H. *Nature* **2000**, *406*, 382.
- (10) Hoertz, P. G.; Mallouk, T. E. *Inorg. Chem.* **2005**, *44*, 6828.
- (11) Kanaizuka, K.; Haruki, R.; Sakata, O.; Yoshimoto, M.; Akita, Y.; Kitagawa, H. *J. Am. Chem. Soc.* **2008**, *130*, 15778.
- (12) Katz, H. E.; Scheller, G.; Putvinski, T. M.; Schilling, M. L.; Wilson, W. L.; Chidsey, C. E. D. *Science* **1991**, *254*, 1485.
- (13) Kurita, T.; Nishimori, Y.; Toshimitsu, F.; Muratsugu, S.; Kume, S.; Nishihara, H. *J. Am. Chem. Soc.* **2010**, *132*, 4524.
- (14) Mondal, P. C.; Yekkonni Lakshmanan, J.; Hamoudi, H.; Zharnikov, M.; Gupta, T. *J. Phys. Chem. C* **2011**, *115*, 16398.
- (15) Motiei, L.; Altman, M.; Gupta, T.; Lupo, F.; Gulino, A.; Evmenenko, G.; Dutta, P.; van der Boom, M. E. *J. Am. Chem. Soc.* **2008**, *130*, 8913.
- (16) Shekhah, O.; Wang, H.; Paradinas, M.; Ocal, C.; Schupbach, B.; Terfort, A.; Zacher, D.; Fischer, R. A.; Wöll, C. *Nat. Mater.* **2009**, *8*, 481.
- (17) Terada, K.; Nakamura, H.; Kanaizuka, K.; Haga, M.; Asai, Y.; Ishida, T. *ACS Nano* **2012**, *6*, 1988.
- (18) Tuccitto, N.; Ferri, V.; Cavazzini, M.; Quici, S.; Zhavnerko, G.; Licciardello, A.; Rampi, M. A. *Nat. Mater.* **2009**, *8*, 41.
- (19) Zacher, D.; Schmid, R.; Wöll, C.; Fischer, R. A. *Angew. Chem., Int. Ed.* **2011**, *50*, 176.
- (20) de Ruiter, G.; Gupta, T.; van der Boom, M. E. *J. Am. Chem. Soc.* **2008**, *130*, 2744.
- (21) Gupta, T.; van der Boom, M. E. *J. Am. Chem. Soc.* **2006**, *128*, 8400.
- (22) Frattarelli, D.; Schiavo, M.; Facchetti, A.; Ratner, M. A.; Marks, T. J. *J. Am. Chem. Soc.* **2009**, *131*, 12595.
- (23) Rashid, A. N.; Erny, C.; Gunter, P. *Adv. Mater.* **2003**, *15*, 2024.
- (24) Motiei, L.; Yao, Y.; Choudhury, J.; Yan, H.; Marks, T. J.; van der Boom, M. E.; Facchetti, A. *J. Am. Chem. Soc.* **2010**, *132*, 12528.
- (25) Gao, S. Y.; Zheng, Z. L.; Lu, J. A.; Cao, R. *Chem. Commun.* **2010**, *46*, 7584.
- (26) Klauk, H.; Zschieschang, U.; Pflaum, J.; Halik, M. *Nature* **2007**, *445*, 745.
- (27) Ortiz, R. P.; Facchetti, A.; Marks, T. J. *Chem. Rev.* **2010**, *110*, 205.
- (28) Shirman, T.; Freeman, D.; Posner, Y. D.; Feldman, I.; Facchetti, A.; van der Boom, M. E. *J. Am. Chem. Soc.* **2008**, *130*, 8162.
- (29) Cerclier, C.; Cousin, F.; Bizot, H.; Moreau, C. L.; Cathala, B. *Langmuir* **2010**, *26*, 17248.
- (30) Perl, A.; Reinhoudt, D. N.; Huskens, J. *Adv. Mater.* **2009**, *21*, 2257.
- (31) Xia, Y.; Whitesides, G. M. *Angew. Chem., Int. Ed.* **1998**, *37*, 550.
- (32) Kumar, A.; Abbott, N. L.; Biebuyck, H. A.; Kim, E.; Whitesides, G. M. *Acc. Chem. Res.* **1995**, *28*, 219.
- (33) Piner, R. D.; Zhu, J.; Xu, F.; Hong, S.; Mirkin, C. A. *Science* **1999**, *283*, 661.
- (34) Andres, C. M.; Kotov, N. A. *J. Am. Chem. Soc.* **2010**, *132*, 14496.
- (35) Scheres, L.; ter Maat, J.; Giesbers, M.; Zuilhof, H. *Small* **2010**, *6*, 642.
- (36) Desiraju, G. R. *Angew. Chem., Int. Ed.* **2007**, *46*, 8342.
- (37) Loi, M. A.; Da Como, E.; Dinelli, F.; Murgia, M.; Zamboni, R.; Biscarini, F.; Muccini, M. *Nat. Mater.* **2005**, *4*, 81.
- (38) Cragg, J. P. *A Practical Guide to Supramolecular Chemistry*; John Wiley & Sons, Ltd: New York, 2005.
- (39) Lehn, J. M. *Supramolecular Chemistry: Concepts and Perspectives*; Wiley-VCH: Weinheim, Germany, 1995.
- (40) Schneider, H. J. *Angew. Chem., Int. Ed.* **1991**, *30*, 1417.
- (41) Sakamoto, R.; Katagiri, S.; Maeda, H.; Nishihara, H. *Coord. Chem. Rev.* **2013**, *257*, 1493.
- (42) Richter, S.; Traulsen, C. H. H.; Heinrich, T.; Poppenberg, J.; Leppich, C.; Holzweber, M.; Unger, W. E. S.; Schalley, C. A. *J. Phys. Chem. C* **2013**, *117*, 18980.
- (43) For a communication on SDA, see: de Ruiter, G.; Lahav, M.; Keisar, H.; van der Boom, M. E. *Angew. Chem., Int. Ed.* **2013**, *52*, 704.
- (44) Wittkopp, P. J.; Kalay, G. *Nat. Rev. Genet.* **2012**, *13*, 59.
- (45) Motiei, L.; Lahav, M.; Freeman, D.; van der Boom, M. E. *J. Am. Chem. Soc.* **2009**, *131*, 3468.
- (46) Wu, K. L.; Ho, S. T.; Chou, C. C.; Chang, Y. C.; Pan, H. A.; Chi, Y.; Chou, P. T. *Angew. Chem., Int. Ed.* **2012**, *51*, 5642.
- (47) Yin, J. F.; Velayudham, M.; Bhattacharya, D.; Lin, H. C.; Lu, K. L. *Coord. Chem. Rev.* **2012**, *256*, 3008.
- (48) Freys, J. C.; Gardner, J. M.; D'Amario, L.; Brown, A. M.; Hammarstrom, L. *Dalton Trans.* **2012**, *41*, 13105.
- (49) Buda, M.; Kalyuzhny, G.; Bard, A. J. *J. Am. Chem. Soc.* **2002**, *124*, 6090.
- (50) Welter, S.; Brunner, K.; Hofstraat, J. W.; De Cola, L. *Nature* **2003**, *421*, 54.
- (51) Kaminker, R.; Motiei, L.; Gulino, A.; Fragalà, I.; Shimon, L. J. W.; Evmenenko, G.; Dutta, P.; Iron, M. A.; van der Boom, M. E. *J. Am. Chem. Soc.* **2010**, *132*, 14554.
- (52) Campagna, S.; Puntoriero, F.; Nastasi, F.; Bergamini, G.; Balzani, V. *Top. Curr. Chem.* **2007**, *280*, 117.
- (53) Kumaresan, D.; Shankar, K.; Vaidya, S.; Schmehl, R. H. *Top. Curr. Chem.* **2007**, *281*, 101.
- (54) Bryant, G.; Fergusson, J.; Powell, H. *Aust. J. Chem.* **1971**, *24*, 257.
- (55) Crosby, G. A.; Demas, J. N. *J. Am. Chem. Soc.* **1971**, *93*, 2841.
- (56) Fujita, I.; Kobayash, H. *Z. Phys. Chem. Neue Folge (Frankfurt)* **1972**, *79*, 309.
- (57) DeLongchamp, D. M.; Kastantin, M.; Hammond, P. T. *Chem. Mater.* **2003**, *15*, 1575.
- (58) Lavallo, P.; Picart, C.; Mutterer, J.; Gergely, C.; Reiss, H.; Voegel, J.-C.; Senger, B.; Schaaf, P. *J. Phys. Chem. B* **2004**, *108*, 635.
- (59) Picart, C.; Mutterer, J.; Richert, L.; Luo, Y.; Prestwich, G. D.; Schaaf, P.; Voegel, J.-C.; Lavallo, P. *Proc. Nat. Acad. Sci.* **2002**, *99*, 12531.
- (60) Porcel, C.; Lavallo, P.; Ball, V.; Decher, G.; Senger, B.; Voegel, J.-C.; Schaaf, P. *Langmuir* **2006**, *22*, 4376.

- (61) Choudhury, J.; Kaminker, R.; Motiei, L.; de Ruiter, G.; Morozov, M.; Lupo, F.; Gulino, A.; van der Boom, M. E. *J. Am. Chem. Soc.* **2010**, *132*, 9295.
- (62) Motiei, L.; Feller, M.; Evmenenko, G.; Dutta, P.; van der Boom, M. E. *Chem. Sci.* **2012**, *3*, 14264.
- (63) Kiessig, H. *Ann. Phys. (Leipzig)* **1931**, *10*, 769.
- (64) Als-Nielsen, J. *Physica* **1986**, *140A*, 2326.
- (65) Evmenenko, G.; van der Boom, M. E.; Kmetko, J.; Dugan, S. W.; Marks, T. J.; Dutta, P. *J. Chem. Phys.* **2001**, *115*, 6722.
- (66) Evmenenko, G.; Stripe, B.; Dutta, P. *J. Colloid Interface Sci.* **2011**, *360*, 793.
- (67) For a review of XPS on self-assembled architectures on surfaces, see: Gulino, A. *Anal. Bioanal. Chem.* **2013**, *405*, 1479.
- (68) Merzlikin, S. V.; Tolkachev, N. N.; Strunskus, T.; Witte, G.; Glogowski, T.; Wöll, C.; Grünert, W. *Surf. Sci.* **2008**, *602*, 755.
- (69) Serroni, S.; Juris, A.; Venturi, M.; Campagna, S.; Resino, I. R.; Denti, G.; Credi, A.; Balzani, V. *J. Mater. Chem.* **1997**, *7*, 1227.
- (70) Venturi, M.; Serroni, S.; Juris, A.; Campagna, S.; Balzani, V. *Top. Curr. Chem.* **1998**, *197*, 193.
- (71) Balzani, V.; Campagna, S.; Denti, G.; Juris, A.; Serroni, S.; Venturi, M. *Acc. Chem. Res.* **1998**, *31*, 26.
- (72) Abruna, H. D.; Denisevich, P.; Umana, M.; Meyer, T. J.; Murray, R. W. *J. Am. Chem. Soc.* **1981**, *103*, 1.
- (73) Denisevich, P.; Willman, K. W.; Murray, R. W. *J. Am. Chem. Soc.* **1981**, *103*, 4727.
- (74) Leidner, C. R.; Murray, R. W. *J. Am. Chem. Soc.* **1985**, *107*, 551.
- (75) Alvarado, R. J.; Mukherjee, J.; Pacsial, E. J.; Alexander, D.; Raymo, F. M. *J. Phys. Chem. B* **2005**, *109*, 6164.
- (76) Araki, K.; Angnes, L.; Toma, H. E. *Adv. Mater.* **1995**, *7*, 554.
- (77) Berchmans, S.; Ramalechume, C.; Lakshmi, V.; Yegnaraman, V. *J. Mater. Chem.* **2002**, *12*, 2538.
- (78) Cameron, C. G.; Pickup, P. G. *J. Am. Chem. Soc.* **1999**, *121*, 11773.
- (79) DeLongchamp, D. M.; Kastantin, M.; Hammond, P. T. *Chem. Mater.* **2003**, *15*, 1575.
- (80) Hjelm, J.; Handel, R. W.; Hagfeldt, A.; Constable, E. C.; Housecroft, C. E.; Forster, R. J. *Inorg. Chem.* **2005**, *44*, 1073.
- (81) Smith, D. K.; Lane, G. A.; Wrighton, M. S. *J. Am. Chem. Soc.* **1986**, *108*, 3522.
- (82) de Ruiter, G.; Motiei, L.; Choudhury, J.; Oded, N.; van der Boom, M. E. *Angew. Chem., Int. Ed.* **2010**, *49*, 4780.
- (83) de Ruiter, G.; Wijsboom, Y. H.; Oded, N.; van der Boom, M. E. *ACS Appl. Mater. Interfaces* **2010**, *2*, 3578.
- (84) For a recent example of electrochromic polymers with three states, see: Sassi, M.; Salamone, M. M.; Ruffo, R.; Mari, C. M.; Pagani, G. A.; Beverina, L. *Adv. Mater.* **2012**, *24*, 2004.
- (85) Deng, H. X.; Doonan, C. J.; Furukawa, H.; Ferreira, R. B.; Towne, J.; Knobler, C. B.; Wang, B.; Yaghi, O. M. *Science* **2010**, *327*, 846.
- (86) Lehn, J. M. *Science* **2002**, *295*, 2400.
- (87) Sknepnek, R.; Anderson, J. A.; Lamm, M. H.; Schmalian, J.; Travesset, A. *ACS Nano* **2008**, *2*, 1259.
- (88) Amoroso, A. J.; Thompson, A. M. W. C.; Maher, J. P.; McCleverty, J. A.; Ward, M. D. *Inorg. Chem.* **1995**, *34*, 4828.
- (89) Li, D.; Swanson, B. I.; Robinson, J. M.; Hoffbauer, M. A. *J. Am. Chem. Soc.* **1993**, *115*, 6975.
- (90) Yerushalmi, R.; Scherz, A.; van der Boom, M. E. *J. Am. Chem. Soc.* **2004**, *126*, 2700.
- (91) Connelly, N. G.; Geiger, W. E. *Chem. Rev.* **1996**, *96*, 877.